Direct PseudoCT Generation for Pelvis PET/MRI Attenuation Correction using Deep Convolutional Neural Networks with Multi-parametric MRI: Zero Echo-time and Dixon Deep pseudoCT (ZeDD-CT)

Andrew P. Leynes[1,2], Jaewon Yang[1], Florian Wiesinger[3], Sandeep S. Kaushik[4], Dattesh D. Shanbhag[4], Youngho Seo[1,2], Thomas A. Hope[1,5], Peder E. Z. Larson[1,2]

[1] *Department of Radiology and Biomedical Imaging, University of California San Francisco, San Francisco, CA, USA*

[2] *UC Berkeley–UCSF Graduate Program in Bioengineering, University of California, Berkeley and University of California, San Francisco, California, USA*

[3] *GE Global Research, Munich, Germany*

[4] *GE Global Research, Bangalore, India*

[5] *Department of Radiology, San Francisco VA Medical Center, San Francisco, CA, USA*

Corresponding author:

Andrew P. Leynes

Department of Radiology and Biomedical Imaging, University of California San Francisco

1700 4th St., Byers Hall Suite 102, San Francisco, California, 94122 USA

Phone: +1 (415) 514-4876 Fax: +1 (415) 514-4451 Email: Andrew.Leynes@ucsf.edu

Word count: 4987 words

Short running title: ZeDD-CT for Pelvis PET/MRI MRAC

ABSTRACT

Accurate quantification of positron emission tomography (PET) uptake depends on accurate attenuation correction in reconstruction. Current magnetic resonance-based attenuation correction methods (MRAC) for body PET imaging use a fat/water map derived from a two-echo Dixon magnetic resonance imaging (MRI) sequence, where bone is neglected. Ultrashort echo-time and zero echo-time (ZTE) pulse sequences can capture bone information. We propose the use of patient-specific multi-parametric MRI consisting of Dixon MRI and proton-density-weighted ZTE MRI to directly synthesize pseudoCT images with the use of a deep learning model: we name this method Zero echo-time and Dixon Deep pseudoCT (ZeDD-CT). **Methods:** Twenty-six patients were scanned using an integrated 3 Tesla time-of-flight PET/MRI system. Helical x-ray computed tomography (CT) images of the patients were acquired separately. A deep convolutional neural network was trained to transform ZTE and Dixon MRI into synthetic CT images (ZeDD-CT). Ten patients were used for model training and sixteen patients were used for evaluation. Bone and soft tissue lesions were identified and the SUV_{max} was measured. The root-mean-squared-error (RMSE) was used to compare the MRAC methods with the ground-truth CTAC. **Results:** A total of 30 bone lesions and 60 soft tissue lesions were evaluated. For bone lesions, there was a factor of 4 reduction of RMSE in PET quantification (RMSE were 10.24% for Dixon PET, and 2.68% for ZeDD PET); for soft tissue lesions, there was a factor of 1.5 reduction of RMSE (RMSE were 6.24% for Dixon PET, and 4.07% for ZeDD PET). **Conclusion:** The ZeDD-CT produces natural-looking and quantitatively accurate pseudoCT images and reduces error in pelvis PET/MRI attenuation correction compared to standard methods.

INTRODUCTION

Reproducible quantification of radiotracer update is central to treatment response, and is typically reported as the standardized uptake values (SUV) (*1,2*). Accurate quantification of uptake depends on accurate attenuation correction, which is a major challenge faced in PET/MRI systems. Uptake quantification is especially important when comparing across different PET/CT and PET/MRI systems, between different vendor systems, or even the same systems with different sets of reconstruction parameters. In PET/CT, 511 keV photon attenuation coefficients can be readily estimated from CT Hounsfield units (HU) using a bilinear model (*3*); however, in PET/MRI, MRI measures nuclear spin properties and lacks photon attenuation information. Thus, it is difficult to infer attenuation information from the MR image intensities, often resulting in inaccurate attenuation correction and associated errors in the PET uptake estimates.

Current commercially available MRAC methods for body PET imaging use a fat/water map derived from a two-echo Dixon MRI sequence, where bone is misclassified as soft-tissue (*4*). Conventional MR imaging approaches do not detect any signal from bone due to its very short T2* relaxation time ($T_2 \approx 0.4ms$ (*5–7*)). Bone attenuation estimation, however, is important particularly in pelvis PET/MRI due to the significant amount of bone, which has the largest photon attenuation among all tissue types. Misclassifying bone in the attenuation coefficient map leads to a large underestimation of PET uptake in and around bone (*8–11*).

Atlas-based methods are commonly used for MRAC in the brain and include bone by registering to an atlas generated from transmission (*12,13*) or CT scans (*14–16*). These methods have been enhanced with the addition of a local pattern-recognition

algorithm (*15*) or a dedicated pulse sequence (*17,18*). The challenge of atlas-based methods is that, by relying on an atlas, they do not completely account for patient-specific variations in bone structure and density.

To capture patient-specific bone information for MRAC, methods based on ultrashort echo-time (*19–23*) and zero echo-time (*11,24–26*) pulse sequences have been proposed. Transverse relaxation rate (R2*) maps have been measured using ultrashort echo-time to estimate continuous-valued attenuation coefficients for bone, however these methods can fail in regions with large magnetic susceptibility differences, such as the sinuses, that may be misclassified as bone. ZTE MRI has also demonstrated excellent bone depiction; an inversely proportional relationship between soft-tissue normalized proton-density-weighted ZTE and CT HU values has been found for the head (*24–26*) and the pelvis (*11*). However, soft-tissues and bone have different corresponding conversion maps so segmentation was necessary to determine the appropriate values to assign in each region.

Deep learning is a machine learning technique that has been demonstrated to be well suited for processing low-level noisy data such as natural images (*27*), and can classify and segment medical images (*28*). Deep learning has also been used for image transformation tasks (*29*) and the MRAC problem can be posed as transforming MR images to synthetic CT images, which has been demonstrated using T1- or T2-weighted images (*30,31*).

Machine learning using artificial neural networks has been used to generate attenuation coefficient maps (*32*). The work used a 3-layer artificial neural network with 154 total parameters and a 6-voxel-neighborhood input. In contrast, deep learning using

deep convolutional neural networks have several layers (typically more than 10) and millions of parameters. With many more layers in deep learning, the input can effectively cover the whole image.

In this paper, we introduce a method using patient-specific multi-parametric MRI consisting of Dixon MRI and proton-density-weighted ZTE MRI to directly synthesize pseudoCT images with a deep learning model. Dixon MRI provides patient-specific continuous-valued attenuation coefficients in soft-tissues (*4*) while ZTE MRI provides the same in bone (*11,24–26*), and deep learning allows a direct and fully-automated conversion of MR images to synthetic CT images (*30,31*). We use this so-called Zero echo-time and Dixon Deep pseudoCT ("ZeDD-CT") for PET image reconstruction and evaluate the impact on radiotracer uptake estimation.

MATERIALS AND METHODS

An overview of the methodology is shown in Figure 1. A deep convolutional neural network was trained with Dixon and ZTE MRI to produce the ZeDD-CT. A Dixon pseudoCT (*4*) was generated as well. The different pseudoCTs were compared with ground-truth CT and the pseudoCT/CT images were converted to attenuation coefficient maps with a bilinear model (*3*). The different maps were then used for PET image reconstruction and data analysis was performed.

Deep Learning

Deep Convolutional Neural Network. The deep convolutional neural network was based on the U-net architecture (*33*), composed of 13 layers in total. A graphical

schematic of the model is shown in Figure 2. The model utilized convolutions (Conv), fractionally-strided convolutions (*34*) (Frac Conv), layer normalization (*35*) (Layer Norm), and rectified linear unit (ReLU) activation functions. The TensorFlow (http://www.tensorflow.org) software package was used to implement and train the neural network.

Inputs to the model were volume patches of the following dimensions: size 32 pixels × 32 pixels × 16 pixels × 3 channels at the Dixon MR image resolution. Each channel was a volume patch of the bias-corrected and soft-tissue normalized proton-density ZTE image, Dixon fractional fat image, and Dixon fractional water image, respectively, at the same spatial location. The ZTE images were resampled with linear interpolation to have the same spatial resolution as the Dixon images. The output was the corresponding ZeDD-CT image with size 32 pixels × 32 pixels × 16 pixels × 1 channel. The network structure leads to an effective input receptive field of at least 19 pixels × 19 pixels × 19 pixels (6858-neighborhood).

Model Training. Model training was performed with an L1-loss, gradient difference loss (GDL), and Laplacian difference loss (LDL) as follows:

$$L_{total} = L_1 + L_{GDL} + L_{LDL}$$

$$L_1 = |\boldsymbol{y} - \widehat{\boldsymbol{y}}|$$

$$L_{GDL} = |\Delta_x\boldsymbol{y} - \Delta_x\widehat{\boldsymbol{y}}|^2 + \left|\Delta_y\boldsymbol{y} - \Delta_y\widehat{\boldsymbol{y}}\right|^2 + |\Delta_z\boldsymbol{y} - \Delta_z\widehat{\boldsymbol{y}}|^2$$

$$L_{LDL} = |\nabla\boldsymbol{y} - \nabla\widehat{\boldsymbol{y}}|^2$$

where y is the ground-truth CT image patch and $\hat{y}$ is the output ZeDD-CT image patch. The gradient difference loss and Laplacian difference loss enforce image sharpness. The Adam optimizer (36) (learning rate = 0.001 halved every 2000 iterations, $\beta_1 = 0.9, \beta_2 = 0.999, \epsilon = 1 \times 10^{-8}$) was used to train the neural network. An L2 regularization ($\lambda = 1 \times 10^{-5}$) on the weights of the network was used. He initialization (37) was used to initialize the weights. A mini-batch of 64 volumetric patches was used for training on one GTX Titan X Pascal (NVIDIA Corporation, Santa Clara, CA, USA) graphics processing unit. There are 6 million parameters that are determined with the training process.

Random crops were extracted from the MR and CT images: to select whether a patch would be used for training, the mean HU value of the corresponding ground-truth CT patch was measured. The probability of the patch being used for training was based on a sigmoidal probability distribution:

$$P_{\text{accept patch}} = \text{sigmoid}(\frac{HU_{mean}}{100} + 700)$$

This was done to reduce the number of patches containing all air. Model training takes approximately 6 hours to reach stability, which occurred at approximately 46,000 iterations at which point the training is stopped.

ZeDD-CT generation. Sequential overlapping 32 pixels $\times$ 32 pixels $\times$ 16 pixels patches at intervals of 8 pixels $\times$ 8 pixels $\times$ 4 pixels were extracted from the MR images and were input to the model. The overlapping patches of the model output were merged by taking

their mean at each voxel location. The ZeDD-CT generation took approximately 3 minutes with a single GTX Titan X Pascal graphics processing unit.

Patient studies

The study was approved by the local Institutional Review Board and all patients signed a written informed consent form.

Patients with pelvic lesions were scanned using an integrated 3 Tesla time-of-flight PET/MRI system (*38*) (SIGNA PET/MR, GE Healthcare, Waukesha, WI, USA). The patient population consisted of 26 patients (Age = 58.1 ± 14.2 years old, 15 males, 11 females): ten (10) patients were used for model training and sixteen (16) patients were used for evaluation. The patient demographics, disease diagnoses, and PET radiotracers of the evaluation dataset are summarized in Supplemental Table 1.

By extracting overlapping patches as described above from the images of the 10 training datasets, roughly 600,000 training examples were used train the neural network.

PET/MRI Acquisition. The PET images were acquired with two radiotracers: ^{18}F-fluorodeoxyglucose and ^{68}Ga-PSMA-11. PET had 600 mm transaxial field-of-view (FOV) and 25 cm axial FOV, with time-of-flight timing resolution of approximately 400 psec. The imaging protocol included a six bed-position whole-body PET/MRI as well as a dedicated pelvic PET/MRI acquisition. The PET data were acquired for 15 min during the dedicated pelvis acquisition, during which time clinical MRI sequences as well as the following MRAC sequences were acquired: Dixon (FOV = 500×500×312 mm, resolution =

1.95×1.95 mm, slice thickness = 5.2 mm, slice spacing = 2.6 mm, scan time = 18 s) and

ZTE MR (cubical FOV = 340×340×340 mm, isotropic resolution = 2×2×2 mm, 1.36ms

readout duration, FA = 0.6°, 4 μs hard RF pulse, scan time = 123 s). The Dixon MRI, ZTE

MRI, and PET image reconstruction (FOV = 600 mm, 2 iterations, 28 subsets, matrix size

= 192×192, 89 slices of 2.78 mm thickness) parameters used were the same as in our

previous work (*11*). Only data from the dedicated pelvic PET/MRI acquisition were used

for this study.

CT Imaging. Helical CT images of the patients were acquired separately on different

machines (GE Discovery STE, GE Discovery ST, Siemens Biograph 16, Siemens

Biograph 6, Philips Gemini TF ToF 16, Philips Gemini TF ToF 64, Siemens SOMATOM

Definition AS) and were co-registered to the MR images using the method outlined below.

Multiple CT protocols were used with variable parameter settings (110-130 kVp, 30-494

mA, rotation time = 0.5 s, pitch = 0.6-1.375, 11.5-55 mm/rotation, axial FOV = 500-700

mm, slice thickness = 3-5 mm, matrix size = 512×512). Pre-processing consisted of filling

in bowel air with soft-tissue HU values and copying arms from the Dixon-derived

pseudoCT due to the differences in bowel air distribution and the CT scan being acquired

with arms up, respectively; more details can be found in section 2.B.2 of our previous

work (*11*).

Image pre-processing and registration. The same methodology in our previous work

(*11*) was used for MRI and CT image pre-processing and co-registration and data

preparation for PET image reconstruction. MRI and CT image pairs were co-registered

using the ANTS (*39*) registration package using the SyN diffeomorphic deformation model with combined mutual information and cross-correlation metrics.

Data Analysis. Standard image error analysis and lesion-based analysis was performed as in our previous work (*11*): the average (μ) and standard deviation (σ) of the error and RMSE were computed over voxels that met a minimum signal amplitude and/or signal-to-noise criteria. Global HU and PET SUV comparisons were only performed in voxels with amplitudes > -200 HU in the ground-truth CT to exclude air, and a similar threshold of > 0.08 cm^{-1} attenuation in the CTAC was used for comparison of AC maps. In addition to standard analysis, summary analysis was performed by co-registering each patient CT to a reference CT image ("atlas-space") with ANTS using the SyN diffeomorphic non-rigid registration model with cross-correlation metric. The reference CT data was manually selected from the patient dataset that had a medium-sized body. This atlas-space transformation was applied for the pseudoCT/CT, AC maps, and PET reconstructions, and the respective difference images with ground-truth. Bone and soft tissue lesions were identified by a board-certified radiologist. Bone lesions are defined as lesions inside bone or with lesion boundaries within 10 mm of bone (*9*). A Wilcoxon signed-rank test was used to compare the SUV_{max} biases compared to CTAC of individual lesions.

To directly compare with our previous work, the data analysis methodology described above was performed on a subset population that was additionally processed using the Hybrid ZTE/Dixon method (*11*). A Friedman test with a Tukey post-hoc test was

used to perform multiple comparisons testing between the Dixon, Hybrid ZTE/Dixon, and ZeDD attenuation correction methods.

RESULTS

ZeDD-CT images

Sample ZeDD-CT images generated are shown in Figure 3. The bone depiction in the femur was comparable to ground-truth CT while there were difficulties in depicting the finer bone structure in the spine. The error across all patients was -36 ± 130 HU and -12 ± 78 HU for the Dixon pseudoCT and ZeDD-CT, respectively. The error for each patient is shown in Supplemental Figure 1.

Attenuation coefficient map analysis

Difference images of the attenuation coefficient maps in the atlas-space are shown in Figure 4. There was significant bone underestimation in Dixon MRAC whereas the error was largely corrected in the ZeDD MRAC. The RMSE across all patients was 5.71% ($\mu = -2.21\%, \sigma = 5.27\%$) and 2.59% ($\mu = -0.69\%, \sigma = 2.50\%$) for the Dixon MRAC and ZeDD MRAC, respectively. The mean underestimation was reduced by a factor of 3 when using the ZeDD MRAC. Additionally, the standard deviation was reduced by a factor of 2. The error for each patient is shown in Supplemental Figure 2.

PET image analysis

Difference images of the reconstructed PET images in the atlas-space are shown in Supplemental Figure 3. The trend was similar with the AC maps: the Dixon PET

underestimated the uptake within and around bony regions and this error was largely corrected in the ZeDD PET. Additionally, uptake within soft tissue regions were slightly underestimated as well. Across all patients, the RMSE was 6.10% ($\mu = -3.40\%, \sigma = 5.07\%$) and 2.85% ($\mu = -1.11\%, \sigma = 2.62\%$) for the Dixon PET and ZeDD PET, respectively. The underestimation bias was reduced by a factor of 3 and the standard deviation was reduced by a factor of 2 when using the ZeDD MRAC. The error for each patient is shown in Supplemental Figure 4.

Lesion analysis

Lesion analysis data are summarized in Figure 5. There were 30 bone lesions and 60 soft tissue lesions across the 16 patient datasets. For bone lesions, there was a factor of 4 reduction of RMSE in PET quantification (RMSE are 10.24% [$\mu = -9.45\%, \sigma = 3.95\%$] for Dixon PET, and 2.68% [$\mu = -1.41\%, \sigma = 2.28\%$] for ZeDD PET; $p_{bone} < 0.0001$); for soft tissue lesions, there was a factor of 1.5 reduction of RMSE (RMSE are 6.24% [$\mu = -4.74\%, \sigma = 4.06\%$] for Dixon PET, and 4.07% [$\mu = -2.39\%, \sigma = 3.29\%$] for ZeDD PET; $p_{soft\ tissue} < 0.0001$). We show the spatial distribution of lesion errors in Supplemental Figure 5.

Hybrid ZTE/Dixon Comparison

Comparisons across a subset of 6 patients between Dixon, Hybrid ZTE/Dixon and ZeDD is summarized in Supplemental Figure 6. The whole-volume RMSE in attenuation coefficient maps are 6.05% ($\mu = -2.79\%, \sigma = 5.37\%$), 6.43% ($\mu = -1.29\%, \sigma = 6.30\%$) and 2.18% ($\mu = -0.56\%, \sigma = 2.11\%$), for Dixon, Hybrid ZTE/Dixon, and ZeDD,

respectively. The whole-volume RMSE in PET images are 6.73% ($\mu = -4.15\%, \sigma = 5.30\%$), 5.78% ($\mu = -2.12\%, \sigma = 5.38\%$) and 2.34% ($\mu = -0.77\%, \sigma = 2.21\%$), for Dixon, Hybrid ZTE/Dixon, and ZeDD, respectively. The bone lesions (N=17) RMSE are 11.27% ($\mu = -10.78\%, \sigma = 3.30\%$), 2.85% ($\mu = -2.52\%, \sigma = 1.33\%$) and 1.59% ($\mu = -0.88\%, \sigma = 1.33\%$), for Dixon, Hybrid ZTE/Dixon, and ZeDD, respectively; and the soft tissue lesions (N=20) RMSE are 6.67% ($\mu = -5.88\%, \sigma = 3.16\%$), 2.82% ($\mu = -2.12\%, \sigma = 1.86\%$) and 3.41% ($\mu = -2.29, \sigma = 2.53\%$), for Dixon, Hybrid ZTE/Dixon, and ZeDD, respectively. For bone lesions, Hybrid ZTE/Dixon and ZeDD are significantly different from Dixon (p<0.001, p<0.001, respectively) and no significant different was found between Hybrid ZTE/Dixon and ZeDD (p=0.27); for soft tissue lesions, the Hybrid ZTE/Dixon and ZeDD are significantly different from Dixon (p<0.001, p<0.001, respectively) and no significant difference was found between Hybrid ZTE/Dixon and ZeDD (p=0.9863).

DISCUSSION

This paper presents a deep convolutional neural network to generate pseudoCT images using combined ZTE and Dixon MRI, named Zero echo-time and Dixon Deep pseudoCT ("ZeDD-CT") for attenuation correction in PET/MRI and analyzes its performance in pelvic lesions. This is the first work to evaluate the performance of a pseudoCT generated from deep learning in the context of pelvis PET/MRI attenuation correction. This is also the first to use patient-specific multi-parametric MRI with deep learning to generate synthetic CT images. The ZeDD method demonstrated improved quantitative uptake for pelvic lesions over the Dixon-based method.

Accurate quantification of PET uptake will likely be important for precision medicine, as it provides more reliable comparisons across scanners, correlation of imaging parameters, and accurate monitoring of treatment response. Although in some cases the attenuation correction error maybe systematic and reproducible for the same patient, a patient may be scanned on different machines within their clinical lifetime. Accurate and precise uptake estimation is also important when developing models that correlate PET parameters with quantitative MR parameters such as from diffusion-weighted imaging. The ZeDD-CT not only improves the PET uptake estimation accuracy, but the precision as well: the standard deviation of PET error in the pelvis was reduced by a factor of 2.

In previous work investigating pelvic osseous lesions, SUV underestimation ranged from 9% to 15% when bone was misclassified (*8–11*), which is in line with the results in this study with Dixon MRAC (underestimation of $9.45 \pm 3.95\%$). Using a model-based approach to incorporate bone attenuation in the body decreased the SUV error in bone lesions to $-2.9 \pm 5.8\%$ (*17*), and our prior work using ZTE-based MRAC with segmentation and regression models had small bone lesion errors of $-3.2 \pm 0.85\%$ (*11*). In the current study, we show bone lesion errors of $-1.41 \pm 2.28\%$ using the ZeDD-CT.

The major improvement in using deep learning is clinical feasibility. We found no significant difference between quantifications based on our previous method (Hybrid ZTE/Dixon-AC) and ZeDD. However, Hybrid ZTE/Dixon relied on a very time-consuming segmentation process that takes 4–6 hours for an experienced user. Other existing methods were automated, but required some human-prescribed parameters (*20–22,25,26*). The deep learning approach is fully-automated and fully-data-driven: MR

images are directly converted to pseudoCT images in a single model. While model training takes several hours, it is only performed once. Once the model is trained, pseudoCT images can be generated in a few minutes immediately after MRI acquisition is completed, making the current method clinically feasible.

Since the PET/MRI and CT acquisitions were done on separate days, there may be errors due to imperfect deformable image registration as well as mismatch of bowel air distributions. The bowel air distributions mismatch makes the comparison for soft-tissue lesions difficult since bowel air is filled in with soft-tissue HU values derived from the Dixon pseudoCT; this may be the reason why the performance of the ZeDD-CT is not as remarkable with soft tissue lesions as with bone lesions.

In a few cases, there were small artifacts where bowel air or skin folds were assigned bone HU values (e.g. Figure 3D), a limitation of the patch-based method: the patch's location inside the body can only be inferred from the structures within the patch. However, these artifacts only occurred in 5 of 16 test patients and correspond to a small fraction of the voxels in the PET imaging volume.

Another limitation is that our model was trained on limited patient demographics: mostly elderly patients being scanned at our institution. Thus, the model we have generated may not be applicable to a pediatric population, who have different bone densities than older patients.

There are arbitrarily many combinations of the elements to produce a deep learning model and new techniques and elements for designing deep learning models are being produced constantly: the deep learning field is the most fast-paced in recent history; the paper by Alex Krizhevsky (40) published in 2012 is considered a "classic" paper in the

field and has over 12,000 citations at the time of this writing. We proposed one of many possible models and demonstrated that utilizing deep learning may lead to fast, fully-automated, and clinically feasible methods for MRAC.

CONCLUSION

We have developed and evaluated the use of a deep convolutional neural network with multi-parametric MRI that produces natural-looking and quantitatively accurate pseudoCT images. The ZeDD-CT been tested in the context of pelvis PET/MRI attenuation correction, and error is reduced compared to standard methods.

DISCLOSURE

REFERENCES

1. Kinahan PE, Fletcher JW. Positron emission tomography-computed tomography standardized uptake values in clinical practice and assessing response to therapy. *Semin Ultrasound CT MRI*. 2010;31:496-505.

2. Wahl RL, Jacene H, Kasamon Y, Lodge MA. From RECIST to PERCIST: Evolving considerations for pet response criteria in solid tumors. *J Nucl Med*. 2009;50:122S-150S.

3. Kinahan PE, Townsend DW, Beyer T, Sashin D. Attenuation correction for a combined 3D PET/CT scanner. *Med Phys*. 1998;25:2046-2053.

4. Wollenweber SD, Ambwani S, Lonn AHR, et al. Comparison of 4-Class and continuous fat/water methods for whole-body, MR-based PET attenuation correction. *IEEE Trans Nucl Sci*. 2013;60:3391-3398.

5. Horch RA, Nyman JS, Gochberg DF, Dortch RD, Does MD. Characterization of 1H NMR signal in human cortical bone for magnetic resonance imaging. *Magn Reson Med*. 2010;64:680-687.

6. Du J, Carl M, Bydder M, Takahashi A, Chung CB, Bydder GM. Qualitative and quantitative ultrashort echo time (UTE) imaging of cortical bone. *J Magn Reson*. 2010;207:304-311.

7. Krug R, Larson PEZ, Wang C, et al. Ultrashort echo time MRI of cortical bone at 7 tesla field strength: A feasibility study. *J Magn Reson Imaging*. 2011;34:691-695.

8. Ouyang J, Chun SY, Petibon Y, Bonab AA, Alpert N, El Fakhri G. Bias atlases for segmentation-based PET attenuation correction using PET-CT and MR. *IEEE Trans Nucl Sci*. 2013;60:3373-3382.

9. Samarin A, Burger C, Wollenweber SD, et al. PET/MR imaging of bone lesions – implications for PET quantification from imperfect attenuation correction. *Eur J Nucl Med Mol Imaging*. 2012;39:1154-1160.

10. Mehranian A, Zaidi H. Impact of Time-of-Flight PET on Quantification errors in MR imaging–based attenuation correction. *J Nucl Med*. 2015;56:635-641.

11. Leynes AP, Yang J, Shanbhag DD, et al. Hybrid ZTE/Dixon MR-based attenuation correction for quantitative uptake estimation of pelvic lesions in PET/MRI. *Med Phys*. 2017;44:902-913.

12. Malone IB, Ansorge RE, Williams GB, Nestor PJ, Carpenter TA, Fryer TD. Attenuation correction methods suitable for brain imaging with a PET/MRI Scanner: A comparison of tissue atlas and template attenuation map approaches. *J Nucl Med*. 2011;52:1142-1149.

13. Montandon M-L, Zaidi H. Atlas-guided non-uniform attenuation correction in cerebral 3D PET imaging. *NeuroImage*. 2005;25:278-286.

14. Sekine T, Buck A, Delso G, et al. Evaluation of atlas-based attenuation correction for integrated PET/MR in human brain – application of a head atlas and comparison to true CT-based attenuation correction. *J Nucl Med*. October 2015:jnumed.115.159228.

15. Hofmann M, Bezrukov I, Mantlik F, et al. MRI-Based attenuation correction for whole-body pet/mri: quantitative evaluation of segmentation- and atlas-based methods. *J Nucl Med*. 2011;52:1392-1399.

16. Wollenweber SD, Ambwani S, Delso G, et al. Evaluation of an atlas-based pet head attenuation correction using PET/CT & MR patient data. *IEEE Trans Nucl Sci*. 2013;60:3383-3390.

17. Paulus DH, Quick HH, Geppert C, et al. Whole-body PET/MR imaging: Quantitative evaluation of a novel model-based MR attenuation correction method including bone. *J Nucl Med*. 2015;56:1061-1066.

18. Koesters T, Friedman KP, Fenchel M, et al. Dixon sequence with superimposed model-based bone compartment provides highly accurate PET/MR attenuation correction of the brain. *J Nucl Med*. 2016;57:918-924.

19. Navalpakkam BK, Braun H, Kuwert T, Quick HH. Magnetic resonance–based attenuation correction for PET/MR hybrid imaging using continuous valued attenuation maps: *Invest Radiol*. 2013;48:323-332.

20. Cabello J, Lukas M, Förster S, Pyka T, Nekolla SG, Ziegler SI. MR-Based attenuation correction using ultrashort-echo-time pulse sequences in dementia patients. *J Nucl Med*. 2015;56:423-429.

21. Juttukonda MR, Mersereau BG, Chen Y, et al. MR-based attenuation correction for PET/MRI neurological studies with continuous-valued attenuation coefficients for bone through a conversion from R2* to CT-Hounsfield units. *NeuroImage*. 2015;112:160-168.

22. Ladefoged CN, Benoit D, Law I, et al. Region specific optimization of continuous linear attenuation coefficients based on UTE (RESOLUTE): application to PET/MR brain imaging. *Phys Med Biol*. 2015;60:8047.

23. Keereman V, Fierens Y, Broux T, Deene YD, Lonneux M, Vandenberghe S. MRI-Based attenuation correction for PET/MRI using ultrashort echo time sequences. *J Nucl Med*. 2010;51:812-818.

24. Wiesinger F, Sacolick LI, Menini A, et al. Zero TEMR bone imaging in the head. *Magn Reson Med*. 2015;75:107-114.

25. Sekine T, Voert EEGW ter, Warnock G, et al. Clinical evaluation of zero-echo-time attenuation correction for brain 18F-FDG PET/MRI: Comparison with atlas attenuation correction. *J Nucl Med*. 2016;57:1927-1932.

26. Yang J, Wiesinger F, Kaushik S, et al. Evaluation of sinus/edge corrected ZTE-based attenuation correction in brain PET/MRI. *J Nucl Med*. May 2017:jnumed.116.188268.

27. LeCun Y, Bengio Y, Hinton G. Deep learning. *Nature*. 2015;521:436-444.

28. Shen D, Wu G, Suk H-I. Deep learning in medical image analysis. *Annu Rev Biomed Eng*. 2017;19:null.

29. Isola P, Zhu J-Y, Zhou T, Efros AA. Image-to-image translation with conditional adversarial networks. *ArXiv161107004 Cs*. November 2016.

30. Nie D, Cao X, Gao Y, Wang L, Shen D. Estimating CT image from MRI data using 3d fully convolutional networks. In: Deep Learning and Data Labeling for Medical Applications. Springer, Cham; 2016:170-178.

31. Han X. MR-based Synthetic CT generation using a deep convolutional neural network method. *Med Phys*. February 2017:n/a-n/a.

32. Santos Ribeiro A, Rota Kops E, Herzog H, Almeida P. Hybrid approach for attenuation correction in PET/MR scanners. *Nucl Instrum Methods Phys Res Sect Accel Spectrometers Detect Assoc Equip*. 2014;734:166-170.

33. Ronneberger O, Fischer P, Brox T. U-Net: Convolutional networks for biomedical image segmentation. In: Medical Image Computing and Computer-Assisted Intervention – MICCAI 2015. Springer, Cham; 2015:234-241.

34. Long J, Shelhamer E, Darrell T. Fully convolutional networks for semantic segmentation. In: 2015 IEEE Conference on Computer Vision and Pattern Recognition (CVPR). ; 2015:3431-3440.

35. Ba JL, Kiros JR, Hinton GE. Layer normalization. *ArXiv160706450 StatML*. July 2016.

36. Kingma DP, Ba J. Adam: A method for stochastic optimization. *ArXiv14126980 Cs*. December 2014.

37. He K, Zhang X, Ren S, Sun J. Delving deep into rectifiers: Surpassing human-level performance on ImageNet classification. In: 2015 IEEE International Conference on Computer Vision (ICCV). ; 2015:1026-1034.

38. Levin CS, Maramraju SH, Khalighi MM, Deller TW, Delso G, Jansen F. Design features and mutual compatibility studies of the time-of-flight PET capable GE SIGNA PET/MR system. *IEEE Trans Med Imaging*. 2016;35:1907-1914.

39. Avants BB, Tustison NJ, Stauffer M, Song G, Wu B, Gee JC. The Insight ToolKit image registration framework. *Front Neuroinformatics*. 2014;8.

40. Krizhevsky A, Sutskever I, Hinton GE. ImageNet classification with deep convolutional neural networks. In: Pereira F, Burges CJC, Bottou L, Weinberger KQ, eds. Advances in Neural Information Processing Systems 25. Curran Associates, Inc.; 2012:1097–1105.
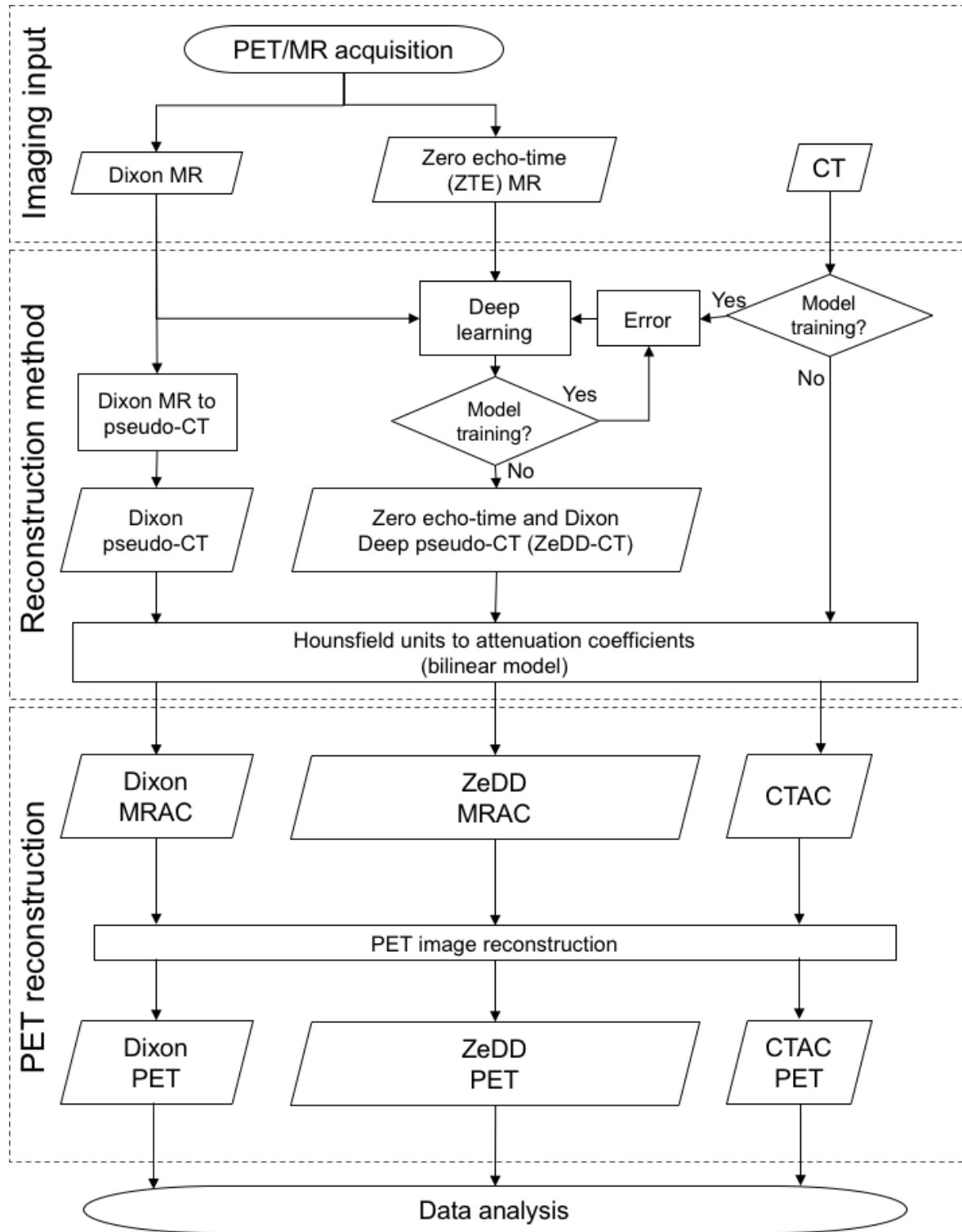
Figure 1. Overview of the methodology.

Figure 2. Deep learning architecture based on U-net (*33*). Each operation in the network is specified in the legend.
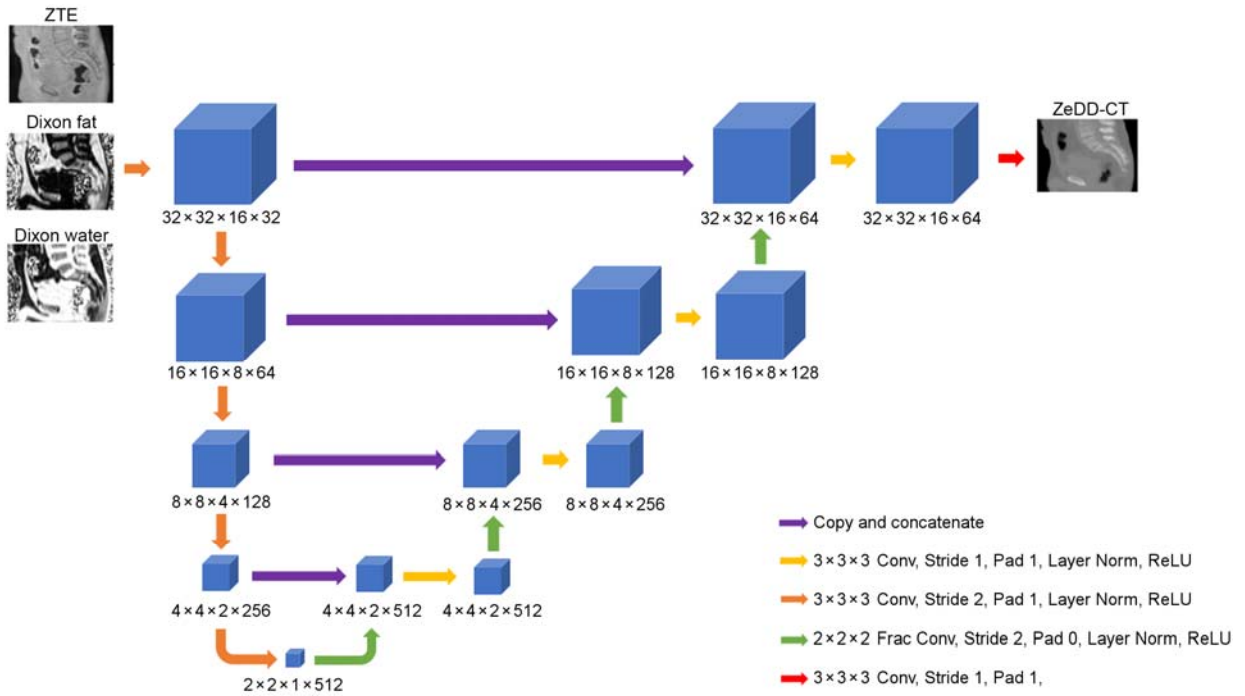
Figure 3. Qualitative comparison of ZeDD-CT with ground-truth CT for several patients. Corresponding MR images are shown in (A). The dark orange arrows with black outline point to a region of bowel air that is captured in the ZeDD-CT. The differences in bowel air distributions between the pseudoCT and ground-truth CT are due to the scans being taken at different times. Bone depiction quality is inspected more closely in (B) and (C). The yellow dashed box indicates the zoomed in regions. Small artifacts where bowel air (orange arrow) and skin folds (yellow arrow) were assigned bone HU values are shown in (D).
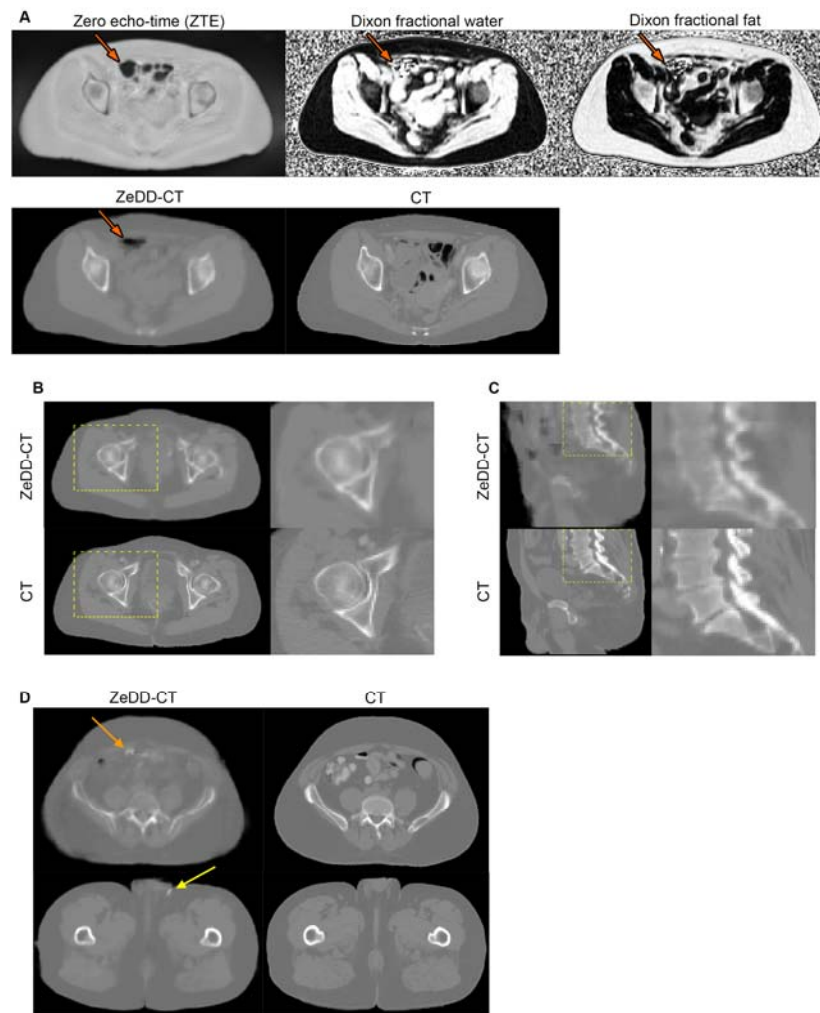
Figure 4. Quantitative comparison of Dixon MRAC and ZeDD MRAC with CTAC in atlas-space. The average CTAC in atlas-space (A) is provided for reference. The average difference maps of the Dixon MRAC and ZeDD MRAC with CTAC are shown in (B). The joint histograms in log-scale (C) show correlation of the attenuation coefficients across the whole volume from all patients. The Dixon MRAC is limited to values between 0.08 cm^{-1} and 0.1 cm^{-1} because only soft-tissue is considered in this approach.
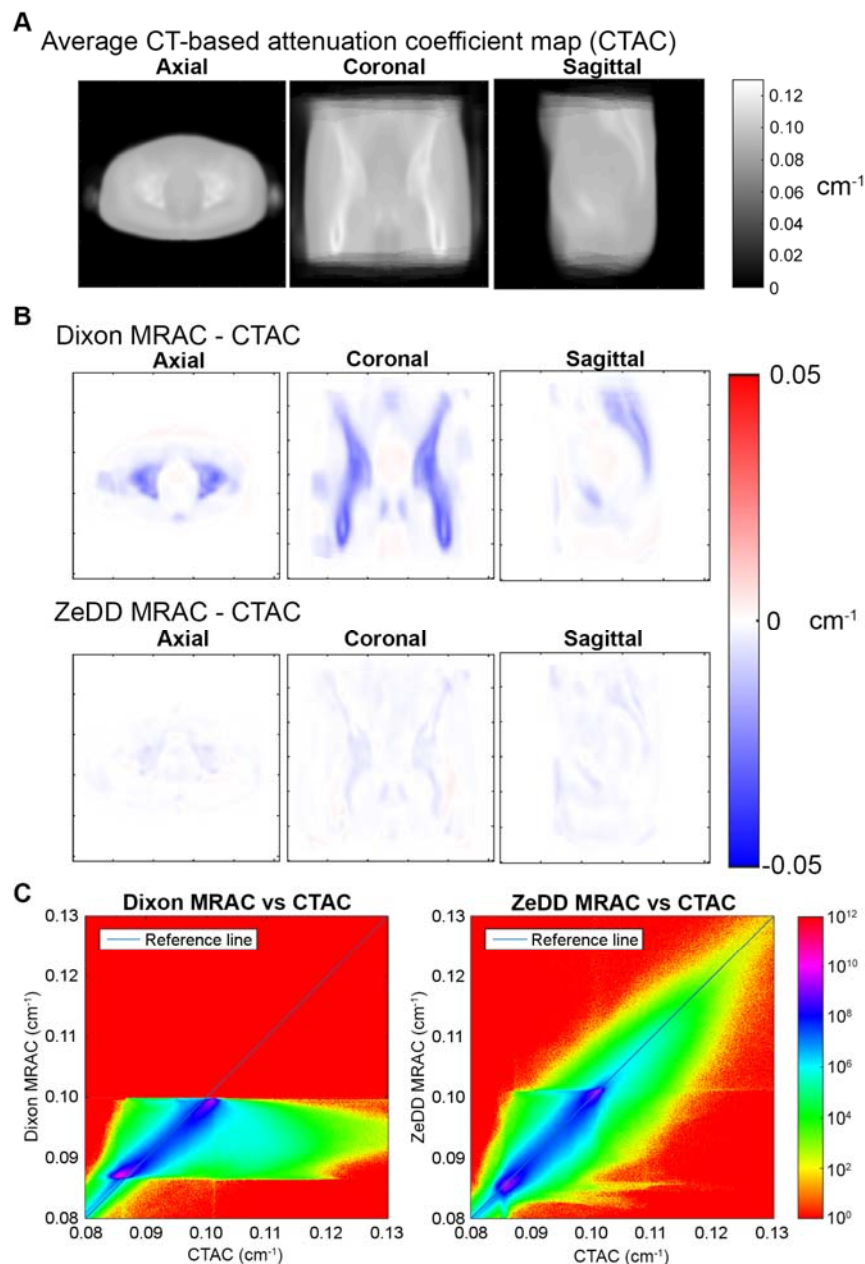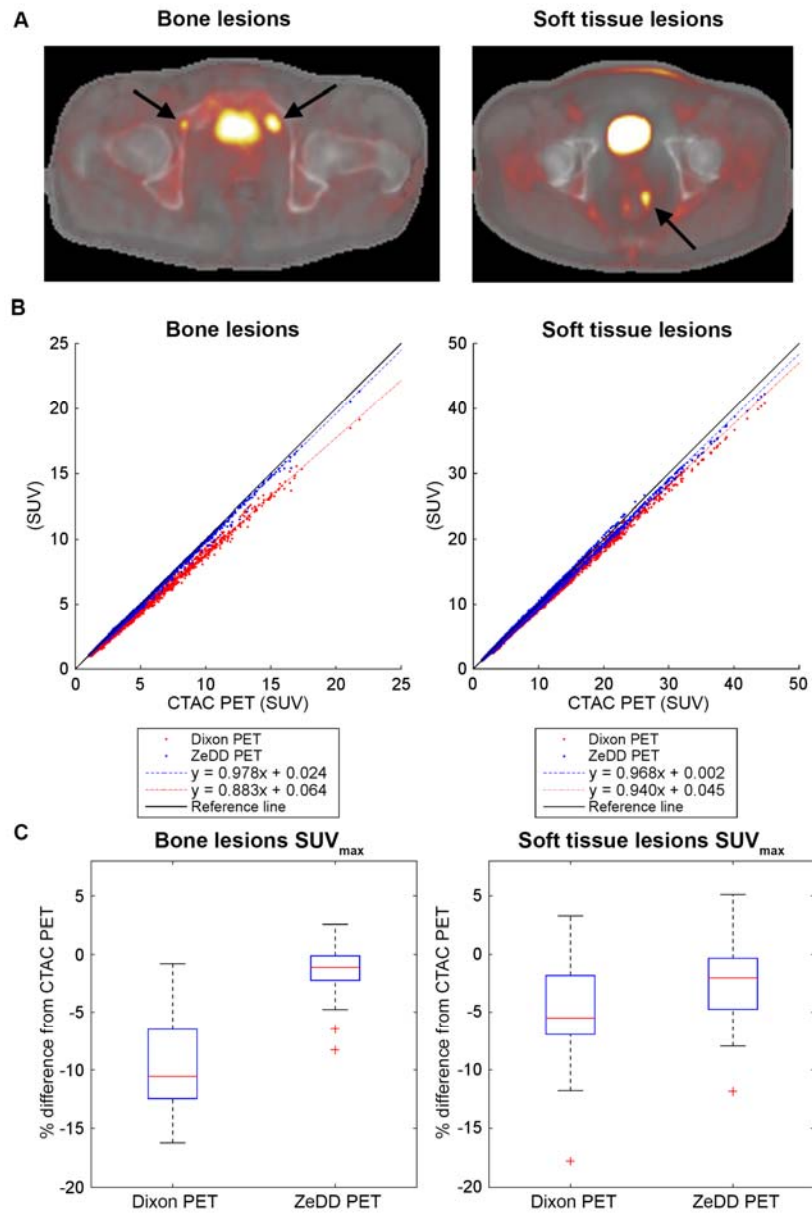
Figure 5. Lesion-based analysis. Maximum standardized uptake values (SUV$_{max}$) were measured in bone lesions and soft tissue lesions (black arrows), with example PET overlays on the ZeDD-CT in (A). The scatter plots (B) and box plots (C) demonstrate the improved accuracy of the deep learning-based MRAC method with ground-truth CTAC compared to Dixon-based MRAC.

Supplemental data for "Direct PseudoCT Generation for Pelvis PET/MRI Attenuation Correction using Deep Convolutional Neural Networks with Multi-parametric MRI: Zero Echo-time and Dixon Deep pseudoCT (ZeDD-CT)"

Supplemental Figure 1. PseudoCT mean error for each patient. For each patient, the Dixon pseudoCT is consistently underestimating the Hounsfield units value. The underestimation is reduced in the ZeDD-CT images. The error bars indicate the standard deviation of Hounsfield units. The ZeDD-CT has lower standard deviation than the Dixon pseudoCT.
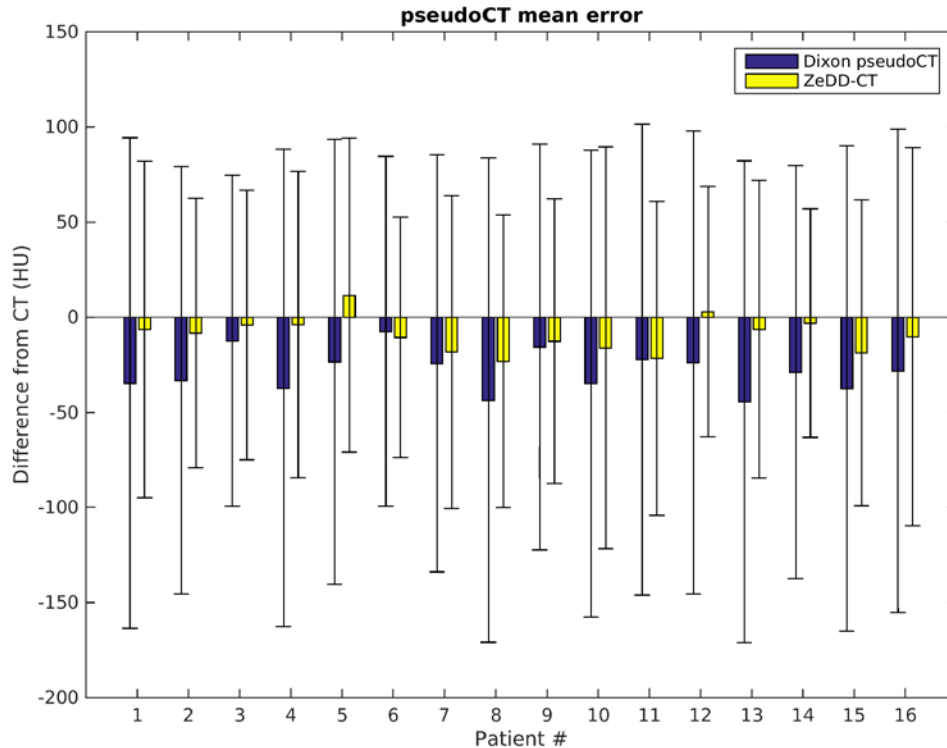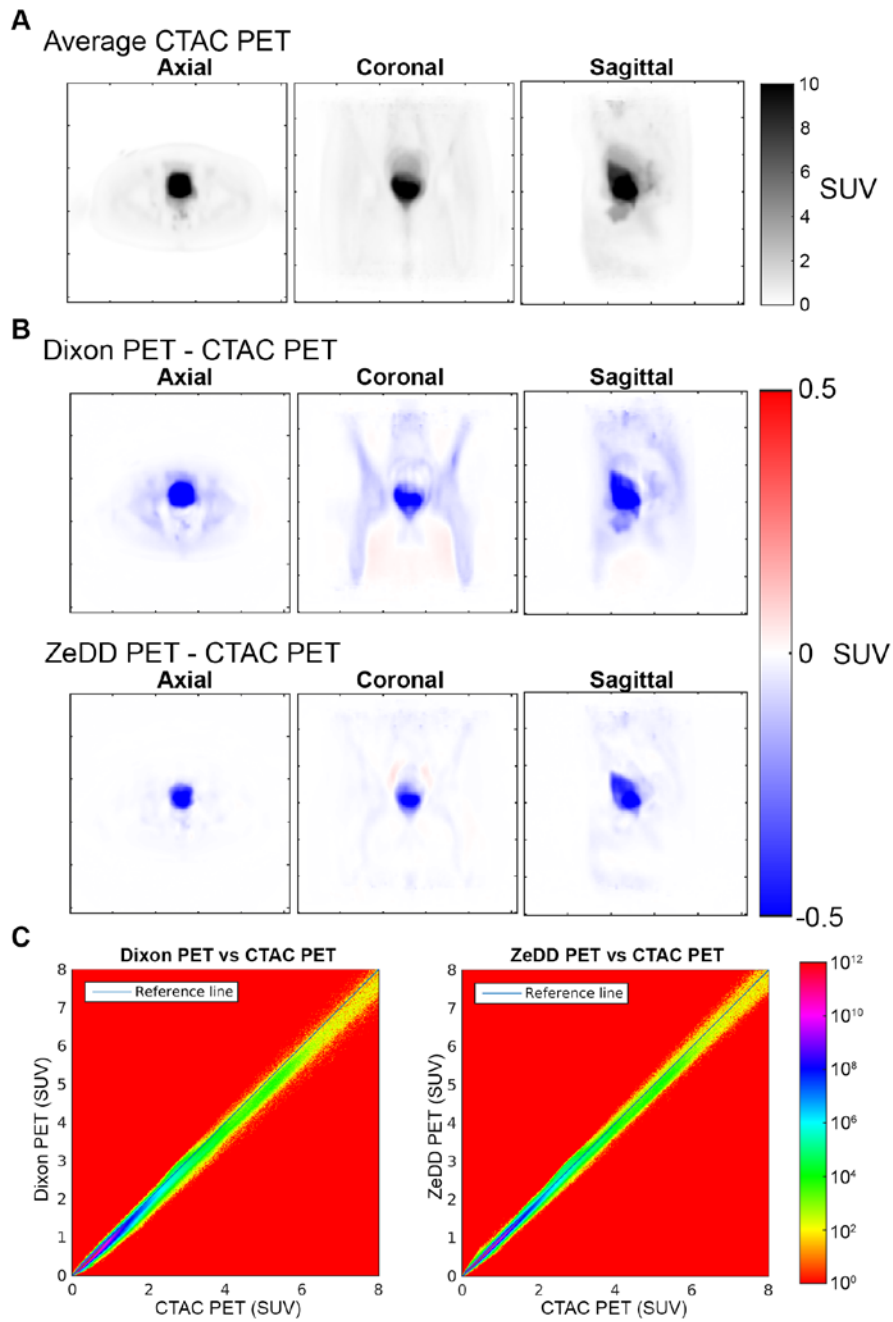
**Supplemental Figure 2.** Attenuation correction map whole-volume error for each patient. For each patient, the Dixon MRAC is consistently underestimating the Hounsfield units value. The underestimation is reduced in the ZeDD MRAC. The error bars indicate the standard deviation of Hounsfield units. The ZeDD MRAC has lower standard deviation than the Dixon MRAC.
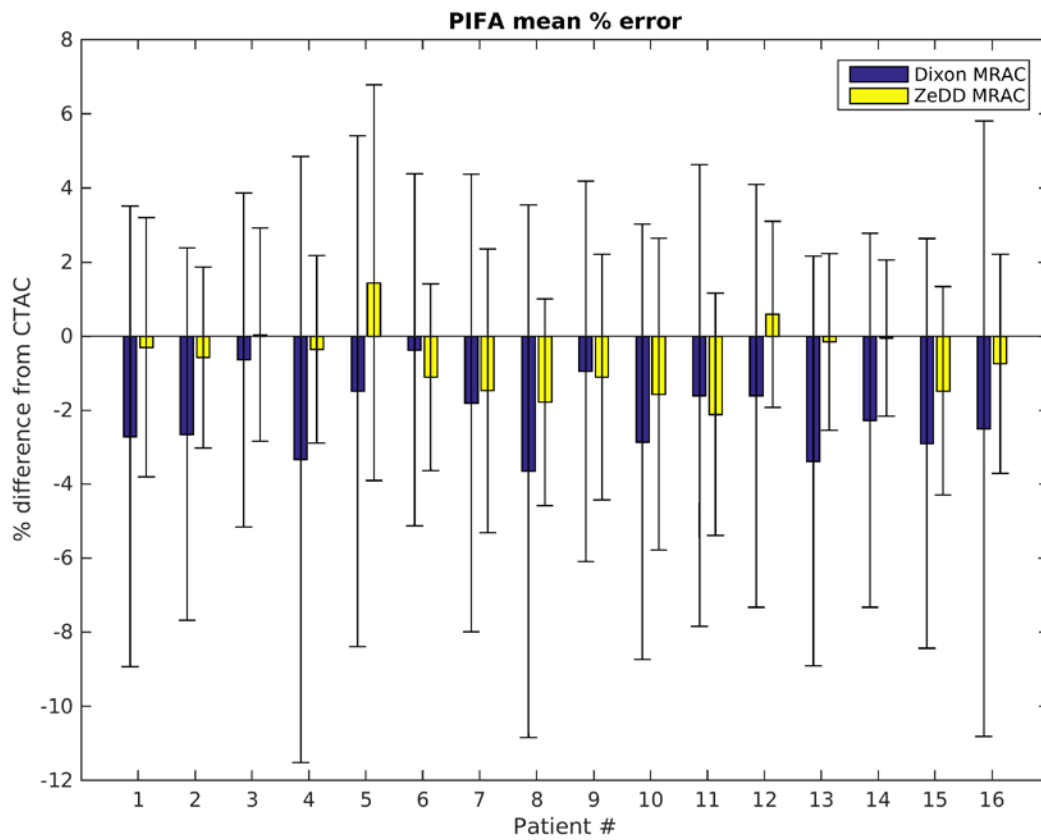
Supplemental Figure 3. Average CTAC PET images from all patients registered to atlas-space (A) and average difference images (B) and joint histograms (C) of Dixon PET and ZeDD PET with CTAC PET. The joint histograms in log-scale (C) show correlation of PET SUV across the whole volume from all patients.

Supplemental Figure 4. PET whole-volume error for each patient. The Dixon PET is consistently underestimating the Hounsfield units value. The underestimation is reduced in the ZeDD PET images. The error bars indicate the standard deviation of Hounsfield units. The ZeDD PET has lower standard deviation than the Dixon PET.
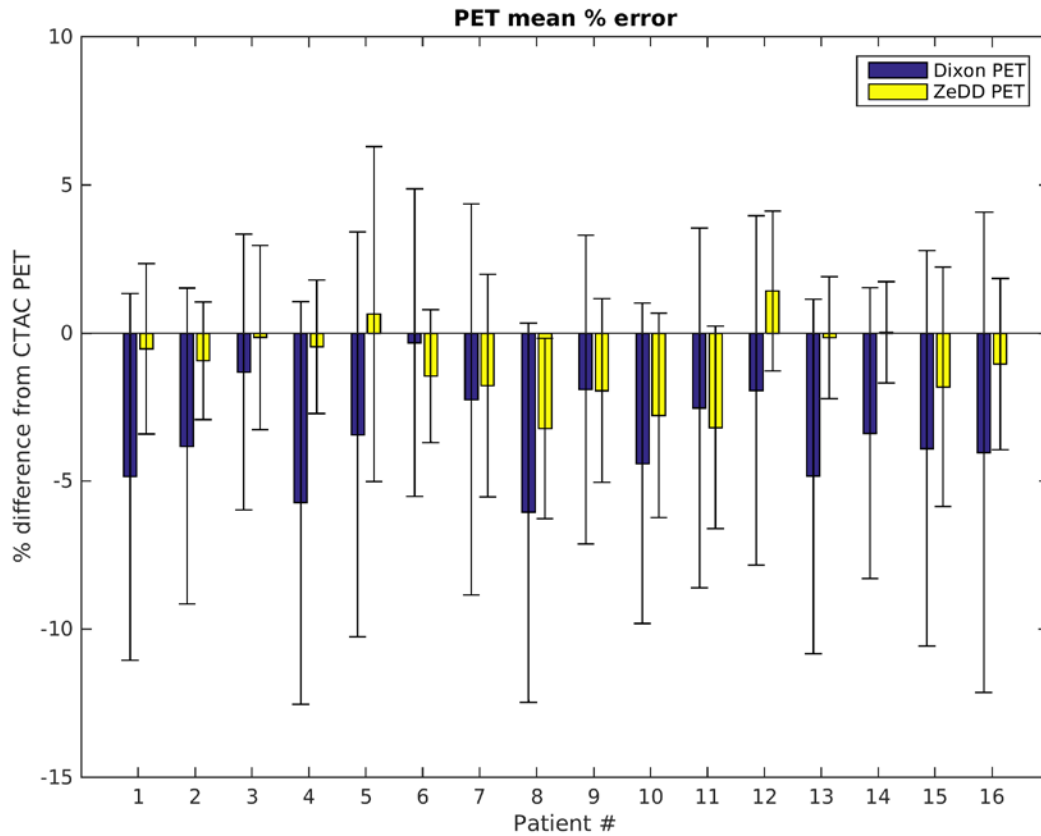
Supplemental Figure 5. Maximum error projections of the lesion error maps for each lesion projected onto the coronal plane are shown. A transparent CT image is overlaid for anatomic reference. The mean bias (μ), standard deviation (σ), and root-mean-squared-error (RMSE) of the uptake in the voxels of each lesion compared to ground-truth are shown below each image. Throughout the whole volume, as with the whole-volume error maps, the lesion uptake was underestimated in the Dixon-based PET.
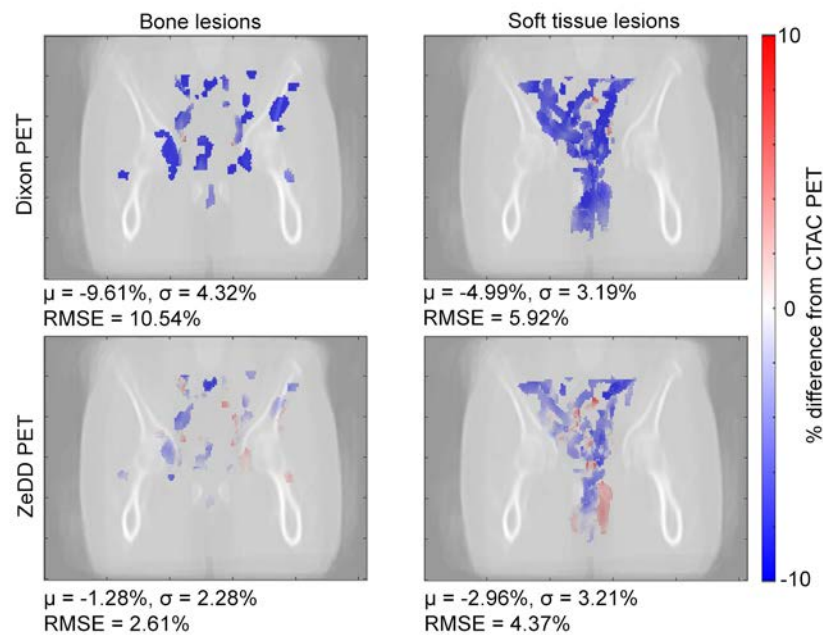
Supplemental Figure 6. Comparative analysis with Hybrid ZTE/Dixon on lesion SUV_{max}. In the subset population of 6 patients, 17 bone lesions and 20 soft tissue lesions were identified. ZeDD produces similar results with Hybrid ZTE/Dixon; both methods demonstrate improvement in SUV_{max} uptake estimation over Dixon and is statistically significant.
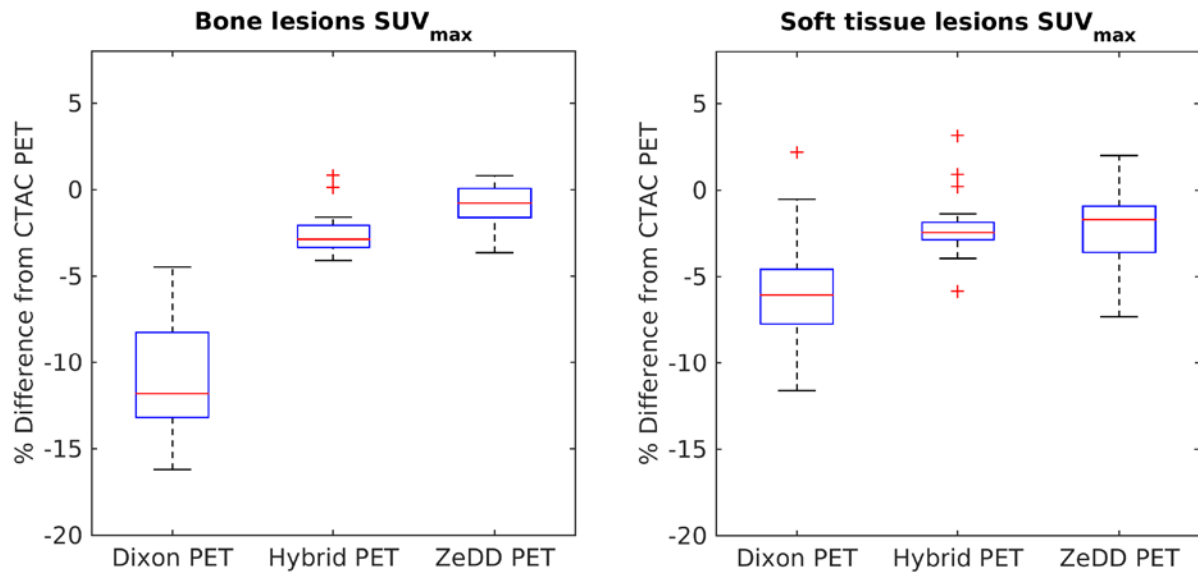
Supplementary Table 1. Patient demographics, disease diagnoses, and PET radiotracers of the test set.

Patient #	Age	Gender	Disease	Radiotracer
1	56	Male	Lung cancer with bone metastases	^{18}F-FDG
2	59	Female	Colon cancer	^{18}F-FDG
3	60	Male	Colon cancer	^{18}F-FDG
4	56	Male	Rectal cancer	^{18}F-FDG
5	58	Male	Rectal cancer	^{18}F-FDG
6	58	Female	Rectal cancer	^{18}F-FDG
7	54	Female	Rectal cancer	^{18}F-FDG
8	69	Male	Prostate cancer	^{68}Ga-PSMA-11
9	70	Male	Prostate cancer	^{68}Ga-PSMA-11
10	60	Female	Cervical cancer	^{18}F-FDG
11	83	Male	Prostate cancer	^{68}Ga-PSMA-11
12	62	Male	Prostate cancer	^{68}Ga-PSMA-11
13	51	Female	Ovarian cancer	^{18}F-FDG
14	62	Male	Rectal Cancer	^{18}F-FDG
15	78	Male	Prostate cancer	^{68}Ga-PSMA-11
16	53	Male	Prostate cancer	^{68}Ga-PSMA-11